Elongated Tetrakaidecahedron Micromechanics Model for Space Shuttle External Tank Foams

Roy M. Sullivan
Glenn Research Center, Cleveland, Ohio

Louis J. Ghosn
Ohio Aerospace Institute, Brook Park, Ohio

Bradley A. Lerch
Glenn Research Center, Cleveland, Ohio

Eric H. Baker
Connecticut Reserve Technologies, Inc., Gates Mills, Ohio

NASA STI Program . . . in Profile

Since its founding, NASA has been dedicated to the advancement of aeronautics and space science. The NASA Scientific and Technical Information (STI) program plays a key part in helping NASA maintain this important role.

The NASA STI Program operates under the auspices of the Agency Chief Information Officer. It collects, organizes, provides for archiving, and disseminates NASA's STI. The NASA STI program provides access to the NASA Aeronautics and Space Database and its public interface, the NASA Technical Reports Server, thus providing one of the largest collections of aeronautical and space science STI in the world. Results are published in both non-NASA channels and by NASA in the NASA STI Report Series, which includes the following report types:

- TECHNICAL PUBLICATION. Reports of completed research or a major significant phase of research that present the results of NASA programs and include extensive data or theoretical analysis. Includes compilations of significant scientific and technical data and information deemed to be of continuing reference value. NASA counterpart of peer-reviewed formal professional papers but has less stringent limitations on manuscript length and extent of graphic presentations.

- TECHNICAL MEMORANDUM. Scientific and technical findings that are preliminary or of specialized interest, e.g., quick release reports, working papers, and bibliographies that contain minimal annotation. Does not contain extensive analysis.

- CONTRACTOR REPORT. Scientific and technical findings by NASA-sponsored contractors and grantees.

- CONFERENCE PUBLICATION. Collected papers from scientific and technical conferences, symposia, seminars, or other meetings sponsored or cosponsored by NASA.

- SPECIAL PUBLICATION. Scientific, technical, or historical information from NASA programs, projects, and missions, often concerned with subjects having substantial public interest.

- TECHNICAL TRANSLATION. English-language translations of foreign scientific and technical material pertinent to NASA's mission.

Specialized services also include creating custom thesauri, building customized databases, organizing and publishing research results.

For more information about the NASA STI program, see the following:

- Access the NASA STI program home page at *http://www.sti.nasa.gov*

- E-mail your question via the Internet to *help@sti.nasa.gov*

- Fax your question to the NASA STI Help Desk at 301–621–0134

- Telephone the NASA STI Help Desk at 301–621–0390

- Write to:
  NASA Center for AeroSpace Information (CASI)
  7115 Standard Drive
  Hanover, MD 21076–1320

Elongated Tetrakaidecahedron Micromechanics Model for Space Shuttle External Tank Foams

Roy M. Sullivan
Glenn Research Center, Cleveland, Ohio

Louis J. Ghosn
Ohio Aerospace Institute, Brook Park, Ohio

Bradley A. Lerch
Glenn Research Center, Cleveland, Ohio

Eric H. Baker
Connecticut Reserve Technologies, Inc., Gates Mills, Ohio

Acknowledgments

Level of Review: This material has been technically reviewed by an expert single reviewer.

Elongated Tetrakaidecahedron Micromechanics Model
for Space Shuttle External Tank Foams

Roy M. Sullivan
National Aeronautics and Space Administration
Glenn Research Center
Cleveland, Ohio 44135

Louis J. Ghosn
Ohio Aerospace Institute
Brook Park, Ohio 44142

Bradley A. Lerch
National Aeronautics and Space Administration
Glenn Research Center
Cleveland, Ohio 44135

Eric H. Baker
Connecticut Reserve Technologies, Inc.
Gates Mills, Ohio 44040

Summary

The results of microstructural characterization studies and physical and mechanical testing of BX–265 and NCFI24–124 foams are reported. A micromechanics model developed previously by the authors is reviewed, and the resulting equations for the elastic constants, the relative density, and the strength of the foam in the principal material directions are presented. The micromechanics model is also used to derive equations to predict the effect of vacuum on the tensile strength and the strains induced by exposure to vacuum. Using a combination of microstructural dimensions and physical and mechanical measurements as input, the equations for the elastic constants and the relative density are applied and the remaining microstructural dimensions are predicted. The predicted microstructural dimensions are in close agreement with the average measured values for both BX–265 and NCFI24–124. With the microstructural dimensions, the model predicts the ratio of the strengths in the principal material directions for both foams. The model is also used to predict the Poisson's ratios, the vacuum-induced strains, and the effect of vacuum on the tensile strengths. However, the comparison of these predicted values with the measured values is not as favorable.

Introduction

The catastrophic loss of the *Space Shuttle Columbia* has spawned numerous engineering and scientific studies focused on improving the engineering infrastructure for external tank spray-on foam insulation (SOFI). Among these are various studies aimed at developing the ability to determine the stress and strain states in foam applications during the shuttle's ascent to space and the ability to predict foam fracture and foam debris liberation. This capability requires a thorough understanding of the foam mechanical and strength behavior in all environments the foam will experience prior to and during ascent.

The mechanical and strength behavior of the SOFI is more complex than most traditional engineering materials, being complicated by the nature of the foam itself. Since the SOFI materials are polymer foams, these properties are temperature dependent. Also, the foams are cellular and must be considered heterogeneous on a scale only slightly smaller than the geometric dimensions of the foam applications. Furthermore, because of the spraying and rising process, the foam microstructure is elongated in the rise direction; thus the foams are, even in the simplest approximation, transversely isotropic (isotropic in the plane transverse to the direction of rising).

Finally, since the SOFI foams are closed-cell foams, they can contain gases at pressures that may not be equivalent to the ambient pressure of the surroundings, resulting in a net tensile or compressive stress in the foam microstructure, which can have a significant influence on their mechanical and strength behavior. Such is the case when foam is placed in a vacuum. The recent experimental work of Stokes (ref. 1) and Morgan (ref. 2) illustrates the effect of exposure to vacuum on the foam behavior. As a result of placing foam specimens in vacuum, Stokes measured an extension in the normal-to-rise direction and a small contraction in the rise direction. Likewise, the experimental results from Morgan reveal that the effect of vacuum is to reduce the ultimate strength in the normal-to-rise direction and to slightly enhance the strength in

the rise direction. Obviously, the ability to simulate the effect of vacuum conditions on the material strain and on the ultimate strength is essential to being able to accurately predict foam failure during flight, as the ambient pressure varies with altitude.

Sullivan et al. (ref. 3) have recently developed a micromechanics model for predicting the mechanical response and strength behavior of nonisotropic, open-cell foams. They expanded the formulation of Zhu et al. (ref. 4) to include nonisotropic foams by using an elongated tetrakaidecahedron as the representative repeating unit cell. Note that a tetrakaidecahedron foam model is commonly referred to as a Kelvin foam model, after Thomson (see ref. 3). The mechanics of deformation of the unit cell led to a set of equations for the modulus, Poisson's ratio, and strength of the foam in the principal material directions. These equations were written in terms of the microstructural dimensions and the strength and stiffness of the solid material. The micromechanics model developed by Sullivan et al. (ref. 3) employs an elongated tetrakaidecahedron unit cell with the most general geometric description, one that is defined with three independent dimensions. Thus, the average microstructure is defined by specifying four dimensions: three to describe the unit cell geometry and one to specify the cell edge cross section. As a result, the micromechanics model requires four input parameters.

In this report, the micromechanics model from Sullivan et al. (ref. 3) is applied to model two rigid polyurethane closed-cell foams used on the space shuttle external tank: BX–265 and NCFI24–124. In the next section, the results from several microstructural characterization studies conducted on BX–265 and NCFI24–124 are presented. The microstructural features are revealed, and the average microstructural dimensions are summarized. Following that, the results of some experimental studies that measured the tensile behavior of these two foams are reported: Results obtained by Morgan (ref. 2) are reviewed, and more recent results obtained by the authors are presented. From these studies, the average stiffness and strength in the principal material directions as well as the measured effect of vacuum on the mechanical behavior and strength are obtained. Next the micromechanics model developed by Sullivan et al. (ref. 3) is reviewed, and the equations for the modulus, Poisson's ratio, and strength in the principal material directions are presented. The micromechanics model is used to derive equations to predict the vacuum-induced strains and the effect of vacuum on the foam tensile strength. Then the model is applied to the BX–265 and NCFI24–124 foams. Using a combination of average measured microstructural dimensions and measured foam properties as the four inputs, the model predicts the remaining microstructural dimensions and the nonisotropic strength ratio for the two foams. The model is also used to predict the foam Poisson's ratios, the effect of vacuum on the tensile strengths, and the vacuum-induced strains, with limited success. Finally, finite element models of elongated tetrakaidecahedron unit cells are used to investigate the cause of the shortcomings with the micromechanics model and its application to the two closed-cell foams. A list of symbols used in this report is provided in the appendix to aid the reader.

Review of Microstructural Characterization Studies

The microstructure of BX–265 and NCFI24–124 foams is illustrated in the photomicrographs shown in figure 1. Both foams are rigid polyurethane closed-cell foams, consisting of cells with an elongated shape. These foams possess a distribution of cell sizes and shapes. Wright and Lerch (ref. 5) measured the average cell dimensions and average number of faces per cell in both BX–265 and NCFI24–124 using a scanning electron microscope (SEM). They found that the average number of faces per cell was 12.4 for BX–265 and 13.7 for NCFI24–124. The average cell height and cell width were 242 and 140 μm, respectively, for BX–265 and 188 and 111 μm, respectively, for NCFI24–124.
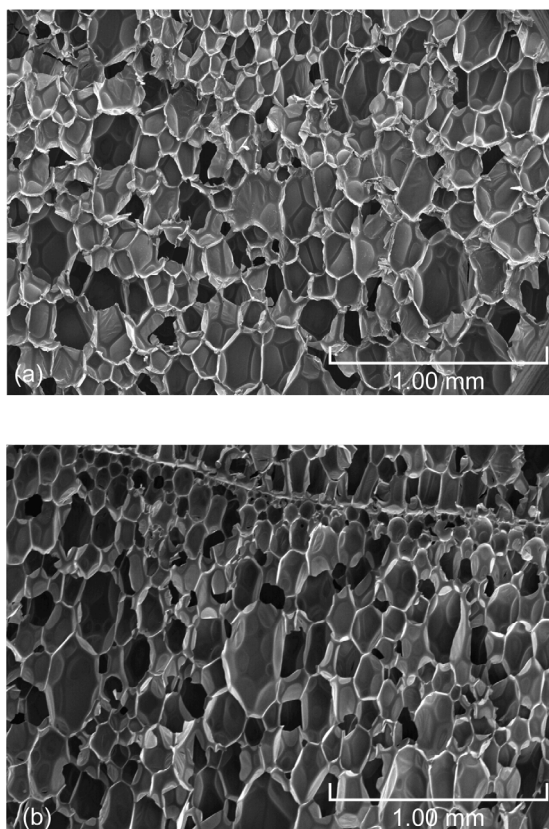

Figure 1.—Photomicrographs of rigid polyurethane closed-cell foams used on the space shuttle external tank. (a) BX–265. (b) NCFI24–124.

More recently, we have measured the average cell dimensions in a series of NCFI24–124 cylinders (P4 cylinders) as well as several BX–265 spray applications obtained from various sources (see table I). The P4 cylinders were initially intended for ballistic impact tests. The results of these more recent characterization efforts are summarized in table I along with the results from Wright and Lerch. Also included in the table is the number of measurements n used to calculate the average.

In view of the microstructural characterization results shown in table I, it appears that the average cell heights in BX–265 and NCFI24–124 are in the range of 150 to 250 µm and that the average cell widths are in the range of 100 to 150 µm. The average ratio of the cell height to cell width lies somewhere in the range of 1.25 to 1.75. Furthermore, if we neglect the microstructural measurements from Wright and Lerch (ref. 5) and consider only the measurements from the more recent studies, we may conclude that the average height of the NCFI cells is greater than the average cell height for the BX–265. This results in a larger average height-to-width ratio for NCFI24–124. Note that there is significant variation in the measured microstructural dimensions between spray batches of the same foam. The variability in the foam microstructure makes it very difficult to establish and apply micromechanics models to study the mechanics of these foams, since the mechanical behavior of foam specimens cut from multiple spray batches may not be uniform.

TABLE I.—SUMMARY OF FOAM MICROSTRUCTURAL CHARACTERIZATION STUDIES

Material	Average cell height[a]		Average cell width[a]		Aspect ratio	Average length of long edges[a]		Average length of short edges[a]		Average edge cross-section radius[b]	
	H, µm	n	D, µm	n		L, µm	n	b, µm	n	r, µm	n
BX–265											
Wright and Lerch (ref. 5)[c]	242	229	140	1573	1.73	--	--	--	--	--	--
Block 1[d]	171	18	107	36	1.60	--	--	--	--	--	--
Block 2[d]	173	18	117	36	1.48	--	--	--	--	--	--
Block 3[d]	158	16	126	36	1.25	--	--	--	--	--	--
Block 1C[e]	215	12	142	36	1.51	--	--	--	--	--	--
Block 2F[e]	216	22	142	46	1.52	89	10	35.5	10	22.5	21
Block 8E[e]	197	15	131	39	1.50	63	3	35	3	18	15
Block KSC–1[f]	223	50	165	150	1.35	--	--	--	--	--	--
Block KSC–2[f]	213	50	136	150	1.57	--	--	--	--	--	--
Block KSC–3[f]	227	50	138	150	1.65	--	--	--	--	--	--
Block KSC–4[f]	201	50	126	150	1.60	--	--	--	--	--	--
Block LOX[g]	193	100	136	100	1.42	--	--	--	--	--	--
NCFI24–124											
Wright and Lerch (ref. 5)[c]	188	208	111	1112	1.69	--	--	--	--	--	--
P4 Cylinders	248	100	142	100	1.75	--	--	--	--	26	27

[a]Dimension found in figure 7; n is number of measurements used to calculate average.
[b]Dimension found in figure 3; n is number of measurements used to calculate average.
[c]Ballistic Impact Test Specimens Supplied by P. Kopfinger (Lockheed Martin Corporation).
[d]Supplied by S. Sparks (NASA Marshall Space Flight Center) March 22, 2005.
[e]Supplied by M. Prince (NASA Marshall Space Flight Center) December 7, 2005.
[f]Supplied by B. Speece (NASA Kennedy Space Center) March 17, 2006.
[g]Supplied by Eloy Martinez (Lockheed Martin at Michoud Assembly Facility) March 14, 2006.

The cell edges are formed by the intersection of multiple faces (fig. 2(a)). The edge cross sections resemble a three-cusp hypocycloid (fig. 2(b)). A three-cusp hypocycloid is the area encompassed by the perimeters of three close-packed circles of equal radius r, arranged as shown in figure 3. Note that the lines connecting the centers of the circles form an equilateral triangle. These lines are bisected by the cusps of the hypocycloid. From figure 3 it is clear that the radius r is equivalent to the cusp-to-cusp distance. Furthermore, the dimensions of the hypocycloid cross section are completely defined by the value of the cross-section radius r.

The average cross-section radius was measured in the block 2F, 8E, and P4 studies; the average radius values are listed in table I. In addition, the average cusp-to-cusp distance was measured in the spray block 8E study. The average cusp-to-cusp distance was found to be 17 µm, which is close to the average measured cross-section radius of 18 µm. The edge cross-section dimensions are significantly greater than the thicknesses of the cell faces. The thickness of the cell faces in the center of the face (away from the edges) was measured in the spray block 8E study and was estimated to be between 0.1 and 1.0 µm. The faces are too thin to measure with more
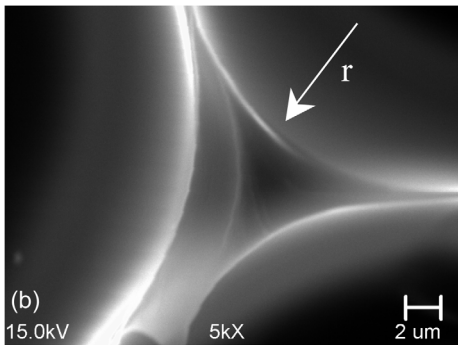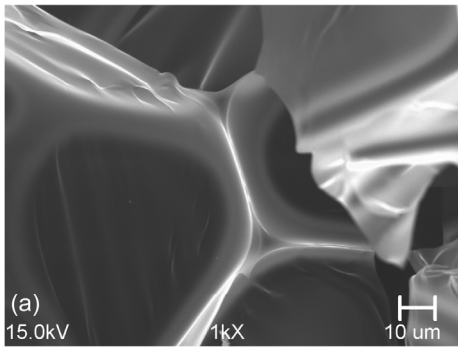
Figure 2.—Photomicrographs of cell edges
  of rigid polyurethane closed-cell foam.
  (a) Edges formed by intersection of multiple
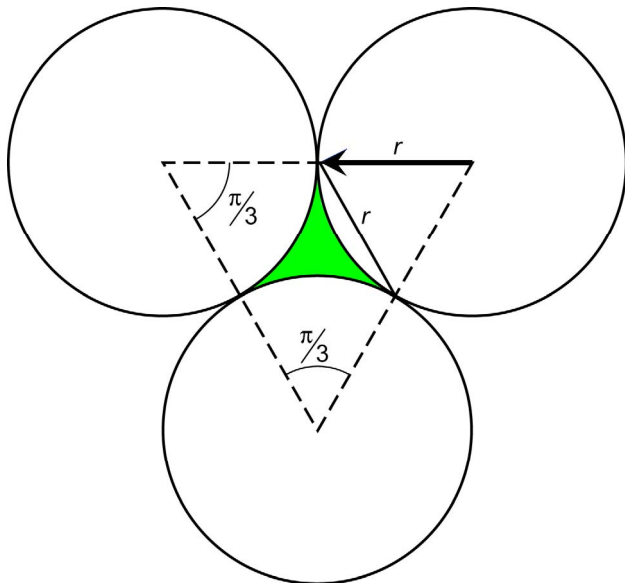 faces. (b) Closeup of edge cross section.

Figure 3.—Three-cusp hypocycloid (shaded area)
  illustrating equivalence of hypocycloid cross-section
  radius r and cusp-to-cusp distance.

certainty by SEM techniques. Studies on other polyurethane foams (refs. 6 and 7) have measured face thicknesses between 1 and 2 μm using light interference patterns. The average lengths of the cell edges were measured in the block 2F and 8E studies. The average lengths are also listed in table I.

The photomicrograph in figure 1(b) shows a portion of a knit line in the upper half of the photo. A knit line is a higher density region that forms between successive spray layers. The cell dimensions are smaller and the cell edges and faces tend to be thicker in the knit lines causing the knit lines to be stronger and stiffer regions of the microstructure.

Review of Experimental Results

The following section describes a series of experimental studies conducted to measure the mechanical behavior and strength of BX–265 and NCFI24–124 foams at standard temperature and pressure conditions as well as in vacuum. The results presented here are from testing conducted primarily at the Glenn Research Center but also include some results from testing conducted at the Marshall Space Flight Center.

Tensile Testing at Glenn Research Center

The room-temperature tensile stress-strain behavior of BX–265 and NCFI24–124 was measured using 50.8-mm- (2-in.-) long parallelepiped specimens. The BX–265 specimens were cut from the LOX block of foam and the NCFI24–124 specimens were cut from the P4 cylinders. The BX–265 specimens had a square cross section with the dimensions of 12.7 by 12.7 mm (0.5 by 0.5 in.), and the NCFI24–124 specimens had a rectangular cross section with the dimensions of 15.24 by 10.16 mm (0.6 by 0.4 in.). In order to measure the material response in both material directions, specimens were cut so that the length dimension was coincident with the rise and perpendicular-to-rise directions.

Samples were glued to platens using epoxy and tested in a standard load frame. A stroke rate of 0.762 mm (0.03 in.)/min was employed. A calibrated 222.4-N (50-lb) load cell was used to measure loads. Displacement was measured using both a linear variable displacement transducer (LVDT) associated with the load frame and a laser micrometer, which read the distance between two flags glued onto the sample. Both methods gave similar values. However, only the strains calculated from the LVDT will be used here, as the LVDT method resulted in a larger signal-to-noise ratio.

The tensile stress-strain curves are shown in figures 4 and 5. Figure 4 shows the BX–265 stress-strain response in the perpendicular-to-rise and rise direction, and figure 5 shows the NCFI24–124 results. Note that the strength and stiffness in the rise direction is considerably higher than in the perpendicular-to-rise direction for both materials. Also, both materials exhibit an initial linear region followed by a nonlinear

response prior to failure. The nonlinear behavior of BX–265 is much more pronounced than for NCFI24–124.

The initial modulus and proportional limit were estimated for each specimen from the stress-strain curves shown in figures 4 and 5. The estimated initial modulus, the estimated proportional limit, and ultimate strength from the BX–265 and NCFI24–124 tensile tests are summarized in tables II and III, respectively. Also listed in tables II and III are the density of the specimen, the number of knit lines in the specimen, and the location of fracture. The average densities of the BX–265 and NCFI24–124 test specimens are 0.0369 and 0.0373 g/cm^3, respectively.

A large number of the BX–265 rise direction specimens failed prematurely, and as a result the strength values associated with these tests are not reported in table II. In all of these tests, the specimens failed at the glue line. In two of these tests (T1 and T5), the adhesive did not fully cure, and this led to premature separation of the glue. All NCFI24–124 specimens failed in the gage section, suggesting that perhaps the sample design having a rectangular cross section was better than the design having a square cross section. The specimen design used here was restricted because of a lack of available material. More studies investigating the effect of the sample design are recommended in order to achieve accurate and reproducible results.
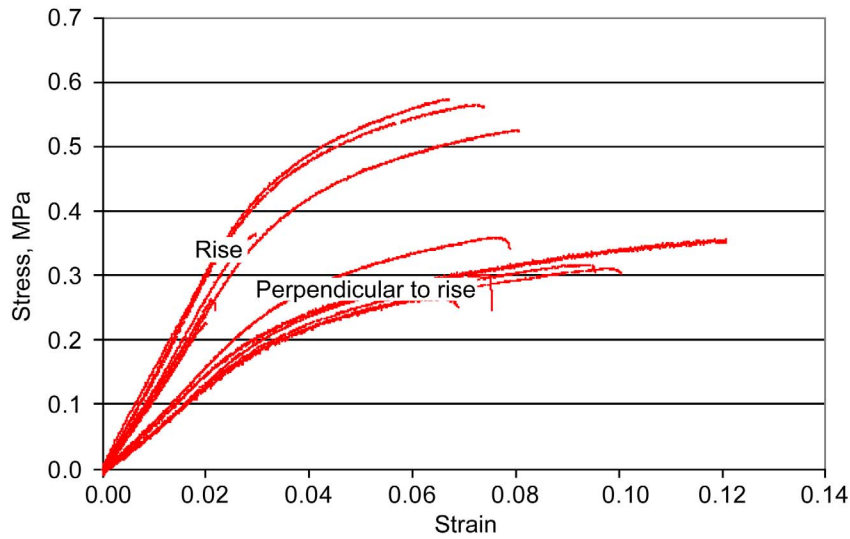

Figure 4.—Room-temperature stress-strain response of BX–265 in rise and perpendicular-to-rise directions.
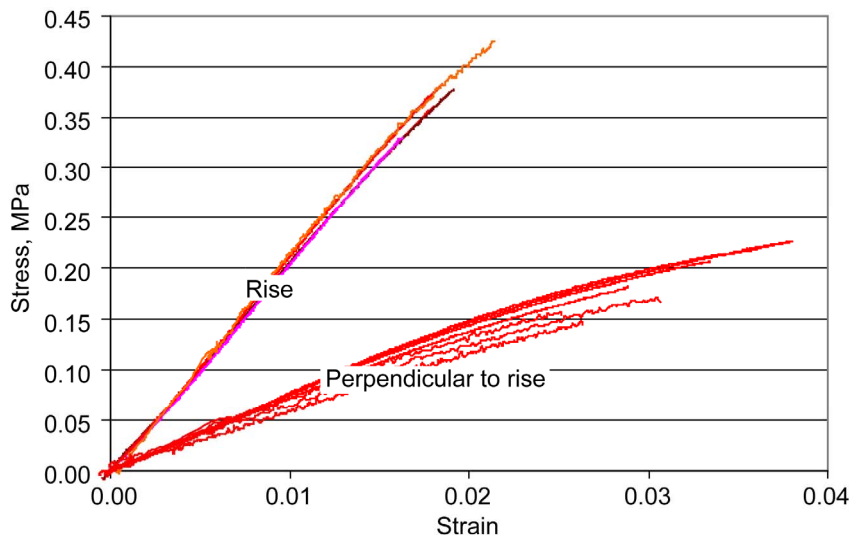

Figure 5.—Room-temperature stress-strain response of NCFI24–124 in rise and perpendicular-to-rise directions.

In some of the tensile tests, the lateral strain in the specimen was also measured in order to determine the Poisson's ratios. The test specimens that were used to measure the Poisson's ratios are identified in tables II and III. Multiple lateral strain measurements were made within the same specimen at various locations within the gage section. The Poisson's ratio for each specimen was calculated from the average lateral strain in the specimen. The measured Poisson's ratios are listed in table IV along with the standard deviations. The notation used to identify the Poisson's ratios in table IV is that the z-axis is in the rise direction and the x- and y-axes are in the perpendicular-to-rise directions.

TABLE II.—SUMMARY OF BX–265 TENSILE TESTING RESULTS

Specimen[a]	Density, ρ, g/cm^3	Number of knit lines	Modulus of elasticity, E, MPa	Proportional limit, kPa	Ultimate tensile strength, kPa	Failure location
Perpendicular-to-rise						
L2	0.0405	3.0	8.21	227.5	359.8	Gage
L3	0.0368	2.0	6.82	165.4	301.9	Gage
L4[b]	0.0378	2.0	7.12	179.2	357.1	Gage
L5	0.0368	1.0	6.69	137.9	312.2	Gage
L6–1[b]	0.0362	1.7	6.60	179.2	268.8	Gage
L7	0.0373	1.0	6.71	151.6	316.4	Gage
Average			**7.03**	**173.5**	**319.4**	
Rise						
T1	0.0370	7.5	13.08	--	--	Glue line
T2	0.0376	8.5	15.47	324.0	575.6	Gage
T3	0.0357	6.5	12.66	303.3	526.6	Gage
T4	0.0353	6.0	13.58	317.1	--	Gage at flag glue line
T5	0.0367	7.0	12.16	--	--	Glue line
T6	0.0376	8.0	14.82	317.1	565.2	Gage
T7[b]	0.0337	3.0	12.33	--	--	Glue line
T8[b]	0.0370	4.0	14.14	--	--	Glue line
Average			**13.53**	**315.4**	**555.8**	
BX Average	**0.0369**					

[a]Tensile specimens from LOX block.
[b]Specimen used for Poisson's ratio measurements.

TABLE III.—SUMMARY OF NCFI24–124 TENSILE TESTING RESULTS

Specimen[a]	Density, ρ, g/cm^3	Number of knit lines	Modulus of elasticity, E, MPa	Proportional limit, kPa	Ultimate tensile strength, kPa	Failure location
Perpendicular-to-rise						
L1	0.0367	2.1	7.09	131.0	182.7	Gage
L2	0.0393	2.2	7.53	103.4	227.5	Gage
L3	0.0385	2.6	7.49	110.3	208.2	Gage
L4	0.0382	2.8	7.73	117.2	220.6	Gage
L5[b]	0.0369	2.0	6.54	75.8	148.2	Gage
L5–2[b]	0.0369	2.0	6.56	117.2	157.8	Gage
L6–4[b]	0.0370	2.0	6.52	124.1	172.3	Gage
Average			**7.07**	**111.3**	**188.2**	
Rise						
T1	0.0367	7.0	20.35	220.6	360.5	Gage
T2	0.0350	7.0	20.27	255.0	377.7	Gage
T3	0.0364	8.0	19.90	248.1	330.2	Gage
T4	0.0364	8.0	20.95	248.1	382.6	Gage
T6[b]	0.0390	4.0	22.52	282.6	426.0	Gage
Average			**20.80**	**250.9**	**375.4**	
NCFI average	**0.0373**					

[a]Tensile specimens from P4 cylinders.
[b]Specimen used for Poisson's ratio measurements.

TABLE IV.—SUMMARY OF MEASURED
POISSON'S RATIOS

	Specimen	Average measured Poisson's ratio	Standard deviation
BX–265 (LOX block)			
v_{xy}	L6–1	0.355	0.06
v_{xz}	L4	0.273	0.0007
v_{zx}	T7	0.536	0.29
v_{zx}	T8	0.675	0.17
NCFI24–124 (P4 cylinders)			
v_{xy}	L6–4	0.382	0.14
v_{xz}	L5	0.183	0.04
v_{xz}	L5–2	0.160	0.03
v_{zx}	T6	0.641	0.10

TABLE V.—STRENGTH AND STIFFNESS
RATIOS FROM TENSILE TEST RESULTS

Foam	Stiffness ratio	Proportional limit ratio	Ultimate tensile strength ratio
BX–265 (LOX block)	1.92	1.82	1.74
NCFI24–124 (P4 cylinders)	2.94	2.25	1.99

The ratio of the modulus in the rise direction to that in the perpendicular-to-rise direction as well as the ratio of the strengths in the two material directions is indicative of the extent to which the average cell is elongated as a result of the spraying. The stiffness and strength ratios were calculated from the average strengths and average moduli listed in tables II and III. These are listed in table V. Since the stiffness and strength ratios for BX–265 are lower than for NCFI24–124, one would expect that an "average" cell in the NCFI24–124 specimens is more elongated than in the BX–265 specimens. This is consistent with the average aspect ratios listed in table I.

Review of NCFI Tensile Testing at NASA Marshall Space Flight Center With and Without Vacuum

Morgan (ref. 2) measured the effect of vacuum conditions on the room-temperature stress-strain behavior of NCFI24–124. The stress-strain behavior in both a 1-atm ambient pressure environment and in vacuum was measured using a 177.8-mm (7-in.) round dogbone specimen. A comparison of the stress-strain response for the two test conditions is shown in figure 6. Note that the stress-strain response shown in figure 6 is similar to the NCFI24–124 response shown in figure 5 and that the average measured ultimate tensile strengths at 1 atm, 420.6 and 185.5 kPa (61 and 26.9 psi), are comparable to the average ultimate tensile strengths listed in table III, 375.4 and 188.2 kPa (54 and 27 psi). The most significant finding from the results obtained by Morgan is that the effect of vacuum on the measured strength of NCFI24–124 is to decrease the foam strength in
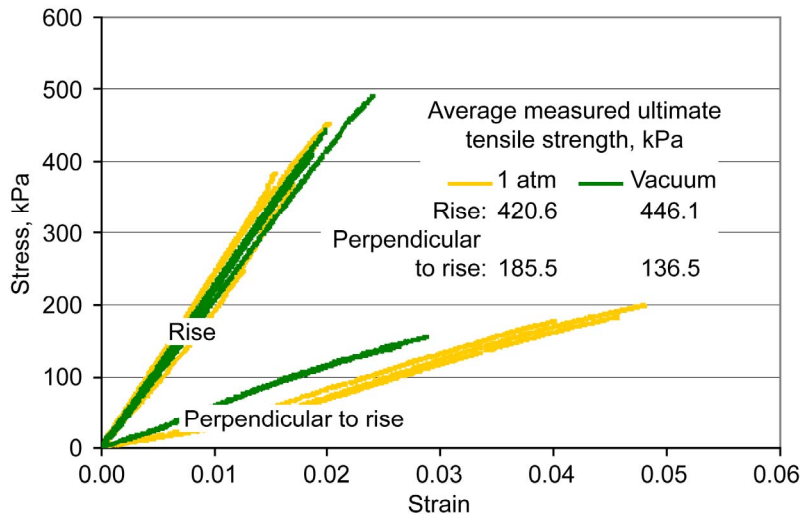
Figure 6.—Stress-strain plot of NCFI24–124 at room temperature in rise and perpendicular-to-rise directions at 1 atm ambient pressure and in vacuum (results from ref. 2).

the perpendicular-to-rise direction 185.5 to 136.5 kPa (26.9 to 19.8 psi) and to enhance (slightly) the strength in the rise direction 420.6 to 446.1 kPa (61.0 to 64.7 psi).

Vacuum Expansion Response

The expansion of the foams as a result of being subjected to a vacuum has been measured at 20 °C at Glenn. Samples were cut from the BX–265 LOX block and from the NCFI24–124 P4 cylinders to dimensions of 12.7 by 12.7 by 50.8 mm (0.5 by 0.5 by 2.0 in.). The specimens were cut so that the 50.8-mm (2.0-in.) length dimension was either parallel to or perpendicular to the rise direction. The tests were conducted using either an optical or a standard dilatometer. The standard dilatometer method uses a probe that rests on one end of the sample. The other end of the probe is connected to an LVDT. The optical system was built in-house and consists of a laser micrometer, which measures the length of the sample. The specimens were placed in the vacuum chamber, the chamber was evacuated to pressures less than 3.45 kPa (0.5 psia), and the lengths of the specimens were recorded.

The average measured strains are listed in table VI along with the standard deviations and the number of samples used to obtain the average. Note that in both foam materials the perpendicular-to-rise direction strain is positive, the rise direction strain is negative, and the perpendicular-to-rise direction strain is over an order of magnitude greater than the absolute value of the rise direction strain. These results are consistent with the vacuum strain results reported previously by Stokes (ref. 1). Indeed, the average strain values shown in table VI are approximately equal to the values measured by Stokes.

TABLE VI.—VACUUM-INDUCED STRAIN[a]

	BX–265 (LOX block)		NCFI24–124 (P4 cylinders)	
	Perpendicular-to-rise	Rise	Perpendicular-to-rise	Rise
Average strain	0.0067	–0.0005	0.0043	–0.0002
Standard deviation	0.0014	0.0008	0.0015	0.0005
Number of samples	6	10	11	7

[a]At less than 3.45 kPa.

Also note that the standard deviation for the rise direction strain is greater than the absolute value of the average. The large relative standard deviation for the rise direction strain measurement can be explained by comparing the magnitude of the measured displacement with the average cell dimensions. Specifically, for a 50.8-mm- (2.0-in.-) long specimen, a measured strain of 0.0005 equates to a measured displacement of ~25 μm, which is slightly greater than one-tenth the height

of an average cell. This makes it difficult to obtain a consistent rise direction strain measurement.

Elongated Tetrakaidecahedron (Kelvin) Open-Cell Model

The following section describes the micromechanics model from Sullivan (ref. 3) for nonisotropic, open-cell foams. The equations for the elastic constants and strengths in the principal material directions are written in terms of the unit cell dimensions as well as the strength and stiffness of the solid material.

Description of Unit Cell

A tetrakaidecahedron is a 14-sided three-dimensional polyhedron comprising six quadrilateral and eight hexagonal faces, which packs to fill space (ref. 8). Since the foam microstructure is elongated because of the spraying and foaming process, we will use an elongated tetrakaidecahedron (fig. 7) as the repeating unit cell. This shape also packs to fill the space. Note that the z-axis is oriented in the rise direction and the x- and y-axes are in the plane perpendicular to the rise direction. The elongated tetrakaidecahedron shown in figure 7 contains eight hexagonal faces, two horizontal square faces, and four vertical diamond faces. The horizontal square faces have sides of length b, and the diamond faces have sides of length L. The hexagonal faces have four sides with a length L and two sides with length b. The inclination angle θ defines the orientation of the hexagonal faces with respect to the rise direction as well as the obtuse angle of the vertical diamond faces, 2θ.

For an elongated tetrakaidecahedron, there are only three characteristic dimensions. The size and shape are uniquely defined by any three of the five dimensions L, b, θ, H, D, since the height H and width D of the unit cell is related to L, b, and θ according to

$$H = 4L \sin\theta \qquad (1a)$$

$$D = 2L \cos\theta + \sqrt{2}b \qquad (1b)$$

The cell aspect ratio $R = H/D$ is therefore

$$R = \frac{4L \sin\theta}{2L \cos\theta + \sqrt{2}b} \qquad (2)$$

Note that there is a minimum value of θ, below which the unit cell in figure 7 is no longer elongated in the z-direction. This minimum value of θ is a function of the length ratio b/L, since as b/L becomes larger, the value of θ must become larger in order for $H > D$ and thus $R > 1$. Sullivan et al. (ref. 3) showed that the lower bound on θ varies with the ratio b/L according to

$$\theta > \arcsin\left(\frac{\sqrt{2}\,b}{5L} + \frac{\sqrt{2}}{10}\sqrt{10 - \frac{b^2}{L^2}}\right)$$

for
$$0 < \frac{b}{L} < 2\sqrt{2} \qquad (3)$$

In applying an open-cell model to closed-cell foams, we make a simplifying assumption that the faces contribute little to the measured structural response and strength behavior and that the majority of the solid mass is contained in the edges of the cells, where the faces come together. This approach allows us to obtain convenient algebraic expressions for the elastic constants and strength in terms of the foam microstructural dimensions and the solid material properties. In defense of this approach, we note that the microstructural characterization studies reveal that the edges are much thicker than the faces, with the face thickness in the middle of the faces being at least an order of magnitude less than the edge thickness. Thus, the microstructure of the foam is modeled as an assemblage of edges. The edges are assumed to behave like struts, having both axial and bending rigidity. The struts have cross-sectional area A and bending moment of inertia I and are made from a polymer with modulus E and tensile strength σ^s.

Foam Relative Density

The relative density γ is, by definition, the ratio of the foam density to the density of the solid material, $\gamma = \rho/\rho_s$. The relative density may be written in terms of volumes as

$\gamma = V_s/V$, where V_s is the volume occupied by solid matter and V is the total volume of the foam. Using the elongated tetrakaidecahedron shown in figure 7 as a representative volume, the total volume is $V = HD^2$. The edges that form the perimeter of the vertical diamond faces and those of length b that form the perimeter of the horizontal square faces are shared by the adjacent cells. Thus, they contribute only half their cross-sectional area to the repeating unit. All other edges are completely contained within the boundaries of the unit cell. Assuming the cross-sectional area A is the same for all edges and constant along the edge length, then $V_s = 16AL + 8Ab$. Using the relations in equation (1), the relative density may be written as

$$\gamma = \frac{2A(2L+b)}{L\sin\theta\left(2L\cos\theta + \sqrt{2}\,b\right)^2} \qquad (4)$$

Expressions for Foam Elastic Constants

Sullivan et al. (ref. 3) developed equations for the foam elastic constants in terms of the microstructural dimensions L, b, and θ, the solid material modulus E, and the edge cross-section properties. For loading in the perpendicular-to-rise direction, they developed equations for the elastic constants using the repeating unit cell shown in figure 8, which represents one-eighth of the tetrakaidecahedron shown in figure 7. Sullivan et al. developed their equations for loading in the perpendicular-to-rise direction by considering the deformation of the unit cell under the application of a uniaxial stress in
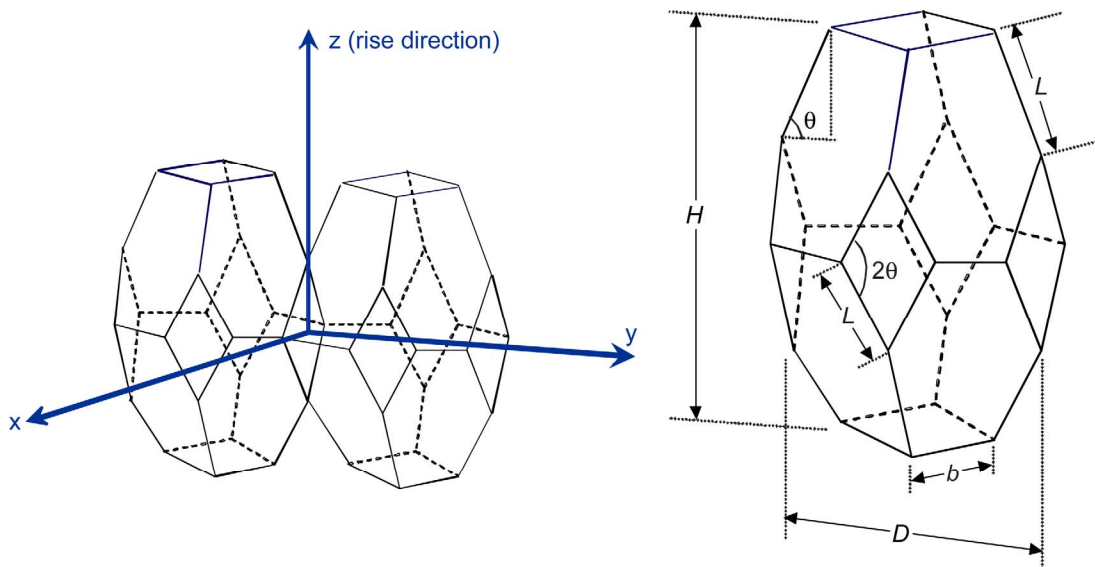

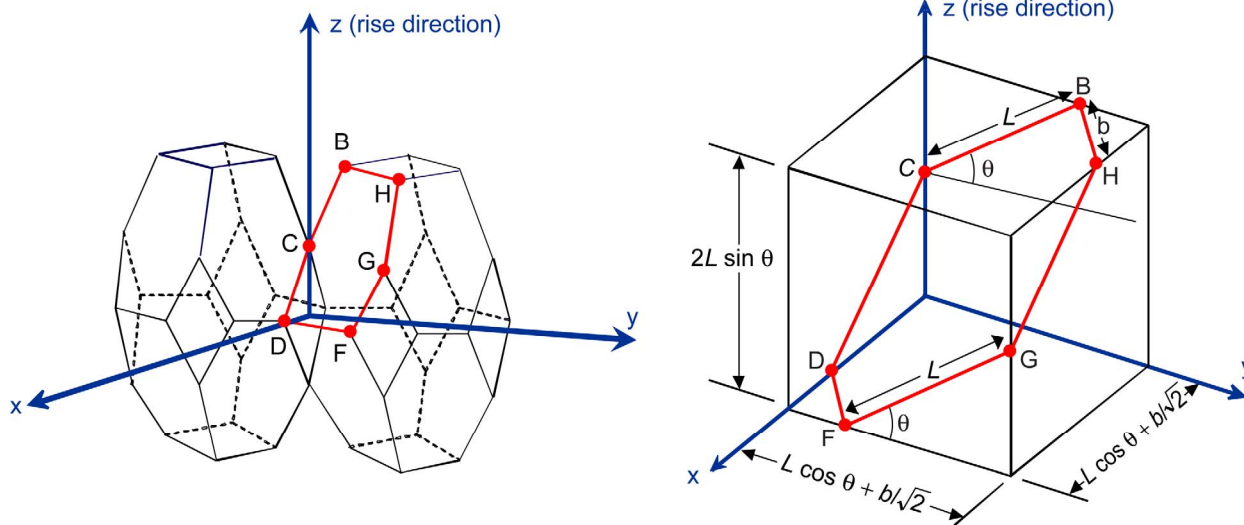Figure 7.—Elongated tetrakaidecahedron repeating unit cell.

Figure 8.—Repeating unit cell for loading in perpendicular-to-rise direction (y-direction).
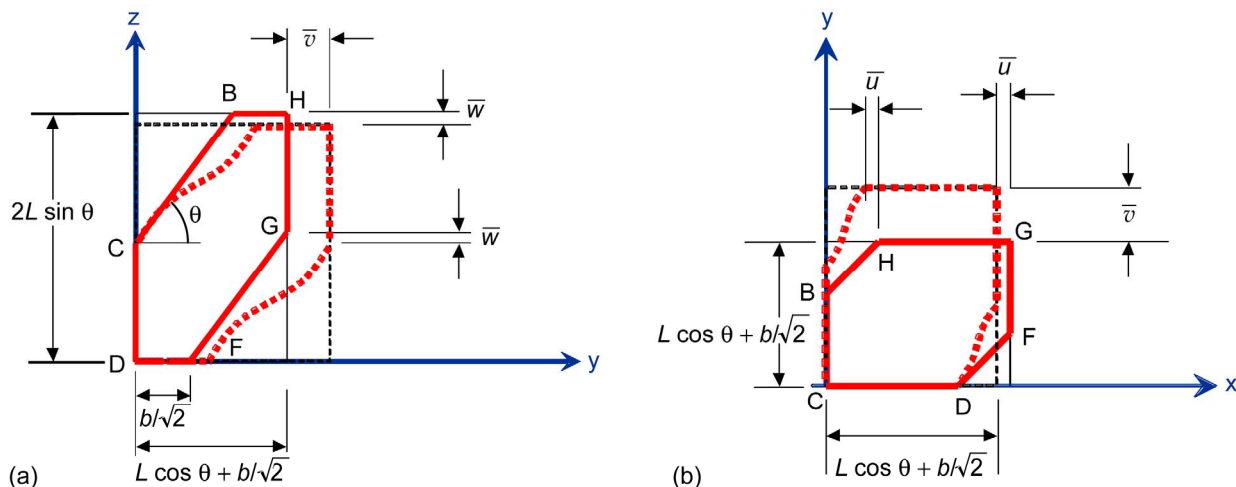

Figure 9.—Unit cell deformation for loading in perpendicular-to-rise direction (y-direction). (a) y,z-plane. (b) x,y-plane.

the y-direction σ_{yy}, which results in an extension in the y-direction and the accompanying contractions in the x- and z-directions. They imposed the symmetry conditions on the member end point displacements

$$
\begin{aligned}
u_B &= u_C = 0 & u_F &= u_G = \overline{u} \\
v_C &= v_D = 0 & v_G &= v_H = \overline{v} \\
w_D &= w_F = 0 & w_B &= w_H = \overline{w}
\end{aligned}
\tag{5}
$$

where the symbols u, v, and w denote the displacements in the x-, y-, and z-directions, respectively, and the symbols $\overline{u}$, $\overline{v}$ and $\overline{w}$ represent the displacements of the unit cell at the unit cell boundaries (fig. 9).

Previous researchers have used circular, square, equilateral triangular, or three-cusp hypocycloid (Plateau borders) shapes to represent the edge cross sections. Note that for any of the four shapes, the moment of inertia of the L-length members (BC and FG) about the neutral axis parallel to the unit cell x-direction I_x^L is equal to the moment of inertia of the b-length members (BH and DF) about the neutral axis parallel to the unit cell z-direction I_z^b, as long as the L- and b-length members have the same cross section. As a result, the expressions for the elastic constants may be developed using $I_x^L = I_z^b = I$.

The equations for Young's modulus and Poisson's ratios were obtained by applying the minimum potential energy theorem to the unit cell deformation, resulting in

$$
E_y = \frac{12EI}{L \sin\theta \left[2L^3 \sin^2\theta + b^3 + \frac{12I}{A}\left(2L\cos^2\theta + b\right)\right]}
\tag{6}
$$

and

$$\nu_{yx} = \frac{b(Ab^2 - 12I)}{12I(2L\cos^2\theta + b) + A(2L^3\sin^2\theta + b^3)} \qquad (7a)$$

$$\nu_{yz} = \frac{(AL^2 - 12I)(2L\cos\theta + \sqrt{2}b)\cos\theta}{2[12I(2L\cos^2\theta + b) + A(2L^3\sin^2\theta + b^3)]} \qquad (7b)$$

Because of symmetry of the unit cell, one can easily recognize that $E_x = E_y$, $\nu_{xy} = \nu_{yx}$, and $\nu_{xz} = \nu_{yz}$.

The application of a perpendicular-to-rise direction stress σ_{yy} induces both an axial load and bending moments in the L-length members (BC and FG) and the b-length members (BH and DF). The maximum bending moment occurs at the member ends, having equal magnitudes but opposite signs at opposite ends of the members: $M_{BC} = -M_{CB}$, $M_{GF} = -M_{FG}$, $M_{BH} = -M_{HB}$, and $M_{DF} = -M_{FD}$. Under the application of a perpendicular-to-rise direction stress σ_{yy}, the axial force and maximum bending moment in the members of length L are, respectively,
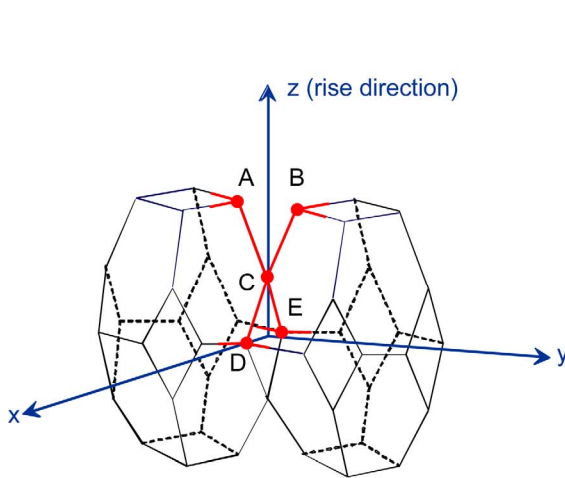
$$N_{BC} = N_{FG} = \sigma_{yy}(2L\cos\theta + \sqrt{2}b)L\cos\theta\sin\theta \qquad (8a)$$

$$M_{BC} = M_{GF} = \frac{\sigma_{yy}}{2}(L\sin\theta)^2(2L\cos\theta + \sqrt{2}b) \qquad (8b)$$

and the axial force and maximum bending moment in the members of length b are, respectively,

$$N_{BH} = N_{DF} = \frac{\sigma_{yy}}{\sqrt{2}}L\sin\theta(2L\cos\theta + \sqrt{2}b) \qquad (9a)$$

$$M_{BH} = M_{DF} = \frac{\sigma_{yy}}{2\sqrt{2}}Lb\sin\theta(2L\cos\theta + \sqrt{2}b) \qquad (9b)$$

To develop the equations for the elastic constants for loading in the z-direction, Sullivan et al. (ref. 3) adopted the unit cell shown in figure 10 and imposed the member end point displacements

$$u_C = v_C = w_C \qquad u_D = -u_E = -\overline{u}$$
$$v_A = -v_B = \overline{v} \qquad w_A = w_B = \overline{w} \qquad (10)$$
$$w_D = w_E = -\overline{w}$$

Application of the minimum potential energy theorem to the unit cell deformation leads to

$$E_z = \frac{24EI\sin\theta}{L^2\left(\cos^2\theta + \frac{12I\sin^2\theta}{AL^2}\right)(\sqrt{2}L\cos\theta + b)^2} \qquad (11)$$

and

$$\nu_{zx} = \nu_{zy} = \frac{\sqrt{2}L^2(AL^2 - 12I)\cos\theta\sin^2\theta}{(12IL\sin^2\theta + AL^3\cos^2\theta)(\sqrt{2}L\cos\theta + b)} \qquad (12)$$

Under the application of a rise direction stress σ_{zz}, the axial force and maximum bending moment in the members of length L are, respectively,

$$N_{BC} = \frac{\sigma_{zz}\sin\theta}{2}(\sqrt{2}L\cos\theta + b)^2 \qquad (13a)$$

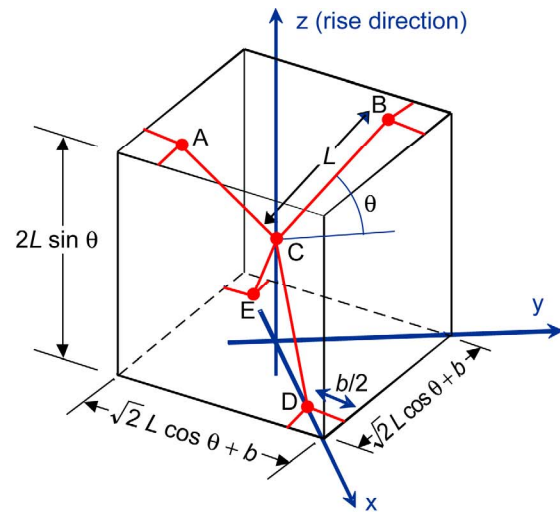$$M_{BC} = -\frac{\sigma_{zz}L\cos\theta}{4}(\sqrt{2}L\cos\theta + b)^2 \qquad (13b)$$

Figure 10.—Repeating unit cell for loading in the rise direction (z-direction).
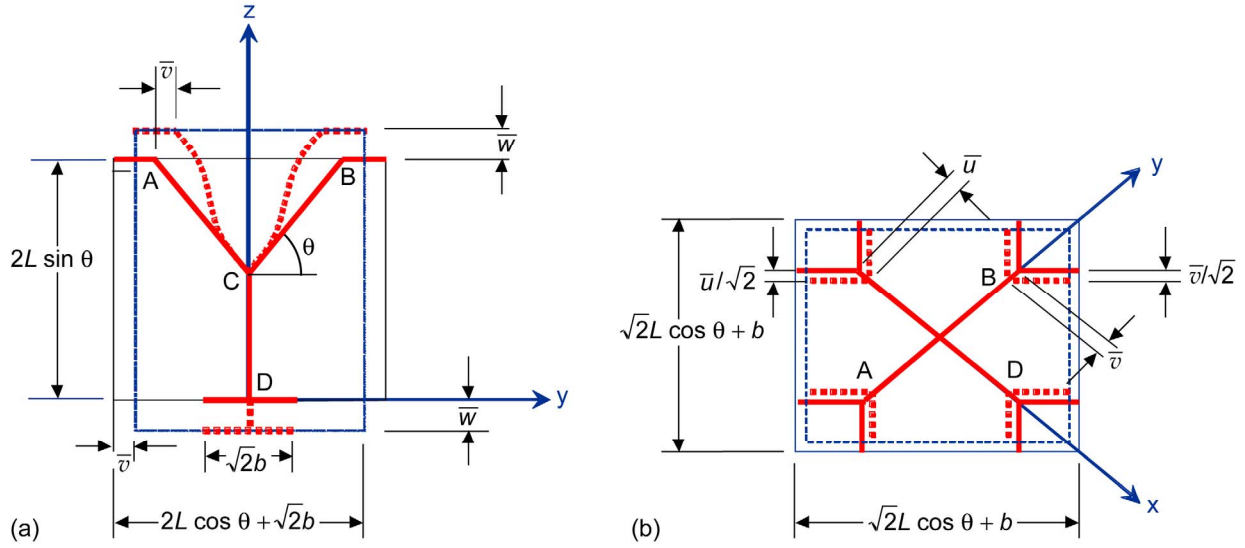
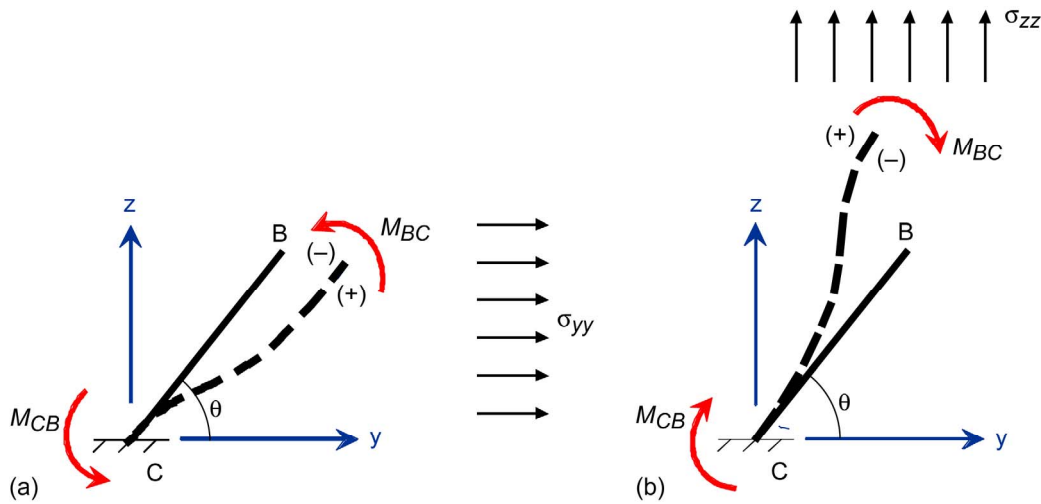Figure 11.—Unit cell deformation for loading in rise direction (z-direction). (a) y,z-plane. (b) x,y-plane.

Figure 12.—Illustration of bending moments *M* at member ends and sign of bending stresses in member BC. (a) y-direction loading. (b) z-direction loading.

Given the restrictions on the member end point displacements, the members of length *b* undergo only rigid body motion (fig. 11) and are therefore unstressed under the application of a rise direction stress. The negative sign appears in the second expression in equation (13b), since the bending moment in struts BC due to σ_{zz} are opposite in sign to the bending moment produced by σ_{yy} (see fig. 12).

Expressions for Foam Tensile Strength in Principal Material Directions

We assume that foam tensile failure occurs when the applied stresses produce a maximum tensile stress in any of the edges, which is equal to the intrinsic strength of the solid material; that is, when $\sigma_{max} = \sigma^s$. Using this assumption, equations can be written for the proportional limit strength or the ultimate tensile strength of the foam. In the former case, σ^s would denote the proportional limit strength of the solid, and in the latter case it would denote the ultimate tensile strength of the solid.

Tensile failure in the y-direction may occur due to failure of either the edges of length *L* or the edges of length *b*. Using $\sigma_{max} = (N/A) \pm (M/S)$, where *S* is the edge section modulus, and the equations (8a) and (8b) for N_{BC} and M_{BC}, respectively, the strength of the foam in the y-direction, based on failure of the edges of length *L*, is given as

$$\sigma_{yy}^s = \frac{\sigma^s}{\left(\dfrac{L\cos\theta\sin\theta}{A} + \dfrac{L^2\sin^2\theta}{2S_x^L}\right)\left(2L\cos\theta + \sqrt{2}b\right)} \qquad (14)$$

In equation (14), S_x^L is the section modulus for the members of length L bending about the section neutral axis, which is parallel to the unit cell x-direction. Likewise, using the equations (9a) and (9b) for N_{BH} and M_{BH}, respectively, the tensile strength of the foam in the y-direction based on failure of the edges of length b is

$$\sigma_{yy}^s = \frac{\sigma^s}{\left(\dfrac{L\sin\theta}{\sqrt{2}A} + \dfrac{Lb\sin\theta}{2\sqrt{2}S_z^b}\right)\left(2L\cos\theta + \sqrt{2}b\right)} \qquad (15)$$

where S_z^b is the section modulus for the members of length b bending about the section neutral axis, which is parallel to the unit cell z-direction.

Equation (14) will always yield a lower estimate of the y-direction strength than equation (15), provided the foam microstructure is such that $S_z^b\left(2S_x^L\cos\theta + AL\sin\theta\right) > S_x^L\left(\sqrt{2}S_z^b + Ab/\sqrt{2}\right)$. If this condition is met, the edges with length L will fail at a lower applied stress σ_{yy} than the edges with length b. Note that if the L-length edges and b-length edges have the same cross section, then $S_x^L = S_z^b$. In what follows, we will assume the two edges have the same cross section and use the symbol S to represent either section moduli. Thus, the condition on the microstructure limiting the perpendicular-to-rise direction strength to failure of the L-length edges becomes

$$2S\cos\theta + AL\sin\theta > \sqrt{2}S + \frac{Ab}{\sqrt{2}} \qquad (16)$$

Regardless of whether the perpendicular-to-rise direction strength is based on failure of the L-length edges or failure of the b-length edges, $\sigma_{xx}^s = \sigma_{yy}^s$ because of symmetry of the unit cell.

Using equations (13), the strength of the foam in the z-direction is

$$\sigma_{zz}^s = \frac{\sigma^s}{\left(\dfrac{\sin\theta}{2A} + \dfrac{L\cos\theta}{4S}\right)\left(\sqrt{2}L\cos\theta + b\right)^2} \qquad (17)$$

Stiffness and Strength Ratios

Defining the stiffness ratio as $R_E = E_z/E_y$, then equations (1), (2), (6), and (11) lead to

$$R_E = \left(\frac{R^2}{4}\right)\frac{\left[2\sin^2\theta + \left(\dfrac{b}{L}\right)^3 + \dfrac{12I}{AL^2}\left(2\cos^2\theta + \dfrac{b}{L}\right)\right]}{\left(\cos^2\theta + \dfrac{12I}{AL^2}\sin^2\theta\right)} \qquad (18)$$

Assuming the perpendicular-to-rise direction strength is limited by failure of the members of length L, then the strength ratio in tension, $R_\sigma = \sigma_{zz}^s/\sigma_{yy}^s$, can be written using equations (1), (2), (14), and (17) as

$$R_\sigma = R\frac{2S\cos\theta + AL\sin\theta}{2S\sin\theta + AL\cos\theta} \qquad (19)$$

Mechanics Under Vacuum: Deformation and Analysis of Tensile Strength

Immediately following foam spraying, rising, and polymer rigidization, the foam cells contain the blowing agent at a pressure near the ambient pressure. If the foam is then placed in air at an ambient pressure of 1 atm, then over time the process of diffusion results in an equilibration of pressures and chemical species, and the cells will eventually contain only air at a pressure of 1 atm.

When foam specimens are excised from foam spray applications and the specimens are subjected to vacuum conditions, there is—in the short term—a differential in pressure between the internal cells and the exterior. This internal pressurization results in a tensile stress acting on the foam microstructure, denoted by $\sigma_{xx}^*, \sigma_{yy}^*$, and σ_{zz}^*. From Hooke's Law, the deformations that result from this internal pressurization are

$$\varepsilon_{xx}^* = \frac{1}{E_x}\sigma_{xx}^* - \frac{\nu_{yx}}{E_y}\sigma_{yy}^* - \frac{\nu_{zx}}{E_z}\sigma_{zz}^* \qquad (20a)$$

$$\varepsilon_{yy}^* = -\frac{\nu_{xy}}{E_x}\sigma_{xx}^* + \frac{1}{E_y}\sigma_{yy}^* - \frac{\nu_{zy}}{E_z}\sigma_{zz}^* \qquad (20b)$$

$$\varepsilon_{zz}^* = -\frac{\nu_{xz}}{E_x}\sigma_{xx}^* - \frac{\nu_{yz}}{E_y}\sigma_{yy}^* + \frac{1}{E_z}\sigma_{zz}^* \qquad (20c)$$

We seek to apply the open-cell, elongated Kelvin model presented in the previous section to simulate the effect of vacuum (and internal pressurization) on the mechanical behavior and strength of the closed-cell space shuttle foams. This approach can be construed as somewhat misguided, since open-cell foams cannot contain an internal pressurization and therefore will not feel any effect from vacuum exposure. However, we will proceed with the understanding that a closed-cell foam containing a pressurized gas can be

sufficiently represented by the open-cell foam model with the applied stresses σ_{xx}^*, σ_{yy}^*, and σ_{zz}^*.

From the equations developed in the previous sections for the Young's moduli and Poisson's ratios and assuming that $\varepsilon_{xx}^* = \varepsilon_{yy}^*$ and $\sigma_{xx}^* = \sigma_{yy}^*$,

$$\begin{Bmatrix} \varepsilon_{yy}^* \\ \varepsilon_{zz}^* \end{Bmatrix} = \begin{bmatrix} B & C \\ F & G \end{bmatrix} \begin{Bmatrix} \sigma_{yy}^* \\ \sigma_{zz}^* \end{Bmatrix} \qquad (21)$$

where

$$B = \frac{2\left[12I\left(L\cos^2\theta + b\right) + AL^3\sin^2\theta\right]}{12EAI} L\sin\theta \qquad (22a)$$

$$C = \frac{\left(12I - AL^2\right)\left(2L\cos\theta + \sqrt{2}b\right)}{24EAI} L\sin\theta\cos\theta \qquad (22b)$$

$$F = \frac{\left(12I - AL^2\right)\left(2L\cos\theta + \sqrt{2}b\right)}{12EAI} L\sin\theta\cos\theta \qquad (22c)$$

$$G = \frac{\left(12I\sin^2\theta + AL^2\cos^2\theta\right)\left(2L\cos\theta + \sqrt{2}b\right)^2}{48EAI\sin\theta} \qquad (22d)$$

The foam stresses resulting from vacuum and internal pressurization will also affect the measured strengths. To calculate the effect of vacuum on the strength, we again assume that foam failure occurs when the foam stresses produce a maximum stress in the polymer struts that is equal to the strength of the polymer. It is also assumed that the condition in equation (16) is always satisfied and the perpendicular-to-rise direction tensile strength is limited by failure of the L-length edges. Thus, for perpendicular-to-rise direction (y-direction) tensile tests conducted in 1-atm ambient pressure, the relation between the strength of the foam and the strength of the polymer struts σ^s follows from equation (14) as

$$\sigma^s = \sigma_{yy}^s L\sin\theta\left(\frac{\cos\theta}{A} + \frac{L\sin\theta}{2S}\right)\left(2L\cos\theta + \sqrt{2}b\right) \qquad (23)$$

where σ_{yy}^s is more specifically identified as the measured strength of the foam in the y-direction under 1-atm ambient pressure.

Under vacuum, the relation between the measured foam strength and the strength of the polymer struts is

$$\begin{aligned} \sigma^s &= \sigma_{yy}^{s,*} L\sin\theta\left(\frac{\cos\theta}{A} + \frac{L\sin\theta}{2S}\right)\left(2L\cos\theta + \sqrt{2}b\right) \\ &+ \sigma_{yy}^* L\sin\theta\left(\frac{\cos\theta}{A} + \frac{L\sin\theta}{2S}\right)\left(2L\cos\theta + \sqrt{2}b\right) \\ &+ \sigma_{zz}^*\left(\frac{\sin\theta}{2A} - \frac{L\cos\theta}{4S}\right)\left(\sqrt{2}L\cos\theta + b\right)^2 \end{aligned} \qquad (24)$$

where $\sigma_{yy}^{s,*}$ denotes the measured foam strength in the y-direction under vacuum test conditions. The negative sign appears inside the brackets in the last term in equation (24), since the bending moment in the L-length members due to σ_{zz}^* is opposite in sign to the bending moment produced by σ_{yy}^*. Furthermore, σ_{xx}^* does not appear in equation (24), since σ_{xx}^* will not produce a stress in struts BC or FG (see fig. 8).

Upon equating equations (23) and (24) and rearranging, the difference between the y-direction strength at 1 atm σ_{yy}^s and the strength in vacuum $\sigma_{yy}^{s,*}$ can be written as

$$\sigma_{yy}^s - \sigma_{yy}^{s,*} = \sigma_{yy}^* + \frac{\sigma_{zz}^*}{R}\frac{2S\sin\theta - AL\cos\theta}{2S\cos\theta + AL\sin\theta} \qquad (25)$$

Once again, note that because of symmetry, $\sigma_{xx}^s - \sigma_{xx}^{s,*} = \sigma_{yy}^s - \sigma_{yy}^{s,*}$.

Using the same approach to assess the z-direction strengths, the difference between the measured strengths at 1 atm σ_{zz}^s and the strength in vacuum conditions $\sigma_{zz}^{s,*}$ can be written as

$$\sigma_{zz}^s - \sigma_{zz}^{s,*} = \sigma_{zz}^* + \sigma_{yy}^* \, R \, \frac{2S\cos\theta - AL\sin\theta}{2S\sin\theta + AL\cos\theta} \qquad (26)$$

Application of Kelvin Model to Simulate Material Behavior

We now attempt to use the equations from the previous section to model the BX–265 and NCFI24–124 material behavior as well as the effect of vacuum on the material behavior that was reported in the Review of Experimental Results section. We will approximate the edge cross sections using a three-cusp hypocycloid. The equations for the cross-sectional area, moments of inertia, and section moduli for a three-cusp hypocycloid cross section are listed in figure 13. Notice that all of the section properties are a function of only the cross-section radius r. Thus, in order to apply the micromechanics model and simulate the material behavior, it is necessary to specify only four microstructural dimensions: any three of the dimensions H, D, L, b, or θ to describe the size and shape of the unit cell and the cross-section radius r to specify the value of the cross-section properties A, I, and S. The four microstructural dimensions may be obtained from a combination of four measured material parameters by manipulating the equations from the previous section. These measured material parameters may be material properties or microstructural dimensions. In this section the measured average cell width, aspect ratio, relative density, and stiffness ratio are used to determine the values of L, b, θ, and r. We then predict the strength ratio, the Poisson's ratios, the vacuum strains, and the effect of vacuum on the ultimate strengths. Given the orientation of the edges with respect to the unit cell, $S_x^L = S_z^b = S_{1-1}$.
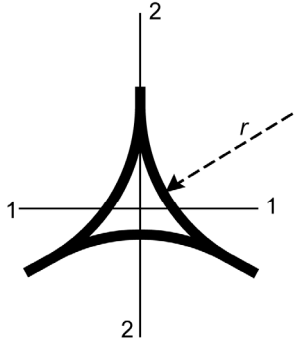
$$A = \left(\sqrt{3} - \frac{\pi}{2}\right)r^2$$

$$I_{1-1} = I_{2-2} = \frac{\left(20\sqrt{3} - 11\pi\right)r^4}{24}$$

$$S_{1-1} = \frac{\left(60 - 11\sqrt{3}\pi\right)r^3}{24}$$

$$S_{2-2} = \frac{\left(20\sqrt{3} - 11\pi\right)r^3}{12}$$

Figure 13.—Equations of cross-section properties for three-cusp hypocycloid edge cross section.

Thus, we used the expression $\left(60 - 11\sqrt{3}\pi\right)r^3/24$ to calculate the value of S in equations (19), (25), and (26).

From equation (2),

$$\frac{b}{L} = \frac{4\sin\theta - 2R\cos\theta}{\sqrt{2}R} \tag{27}$$

Using $D = H/R$ and equation (1), equation (4) can be written as

$$\gamma = \frac{AR^2(2 + b/L)}{8L^2\sin^3\theta} \tag{28}$$

Substituting equation (27) into (28) and making use of the relation $A = C_1 r^2$, where $C_1 = \sqrt{3} - \pi/2$, equation (28) can be rewritten and rearranged as

$$\left(\frac{r}{L}\right)^2 = \frac{4\sqrt{2}\gamma\sin^3\theta}{C_1 R\left(\sqrt{2}R + 2\sin\theta - R\cos\theta\right)} \tag{29}$$

There is also the relation $\dfrac{12I}{AL^2} = C_2\left(\dfrac{r}{L}\right)^2$, where

$C_2 = \dfrac{20\sqrt{3} - 11\pi}{2\sqrt{3} - \pi}$. Substituting this relation in equation (18), we may rewrite equation (18) in the form

$$\left[2R^2 C_2\left(\frac{r}{L}\right)^2 - 4R_E\right]\cos^2\theta$$

$$+ \left[2R^2 - 4R_E C_2\left(\frac{r}{L}\right)^2\right]\sin^2\theta \tag{30}$$

$$+ R^2\left(\frac{b}{L}\right)\left[C_2\left(\frac{r}{L}\right)^2 + \left(\frac{b}{L}\right)^2\right] = 0$$

In order to solve for L, b, θ, and r, we could substitute equations (27) and (29) into equation (30), and using the identity relation $\cos^2\theta = 1 - \sin^2\theta$, obtain an explicit algebraic equation in terms of $\sin\theta$. Using the input values for D, γ, R, and

R_E, the resulting equation can be solved to obtain the value of θ. The resulting equation is, however, quite cumbersome. Instead, we choose to solve the set of equations (27), (29), and (30) in an iterative manner, whereby these equations are solved in series within each iteration.

The standard bisection method (ref. 9) was implemented to solve the set of equations (27), (29), and (30) numerically for θ. Denoting the left-hand side of equation (30) as $f(\theta)$, we note that the true solution for θ according to equation (30) is obtained at $f(\theta) = 0$. The standard bisection method is an iterative method that seeks to solve the set of equations by decreasing the residual value of $f(\theta)$ with each successive iteration such that $f_i(\theta) \to 0$, where i denotes the number of iterations.

The first step in the solution scheme was to make an initial guess at a lower bound θ_l and an upper bound θ_u for the value of the inclination angle θ. Next, the average of θ_l and θ_u was calculated. Using the average of θ_l and θ_u along with the input values for R and γ, equations (27) and (29) were solved to calculate the values of b/L and r/L, respectively. The values of b/L and r/L were then substituted into equation (30), and using the input values for R and R_E, the numerical value of $f(\theta)$ was determined.

The iterative process is facilitated by updating the values of the upper or lower bounds on θ at each iteration step. The sign of the numerical value of $f(\theta)$ determines the new set of lower and upper bounds. If $f(\theta)$ is positive, then the average of θ_u and θ_l was assigned to be the new upper bound. If the value of $f(\theta)$ is negative, then the average was assigned to be the new lower bound. Using the updated upper and lower bounds, a new average was calculated. The new average was used to repeat the process. This process was repeated until the difference in the upper and lower bound average between two successive iterations was less than 10^{-14}. The method converged usually within 30 iterations given an initial bracketed guess for the inclination angle between 40° and 75°.

Once the final value of θ is obtained from the iterative solution, the value of L is determined from $L = RD/4\sin\theta$, and the values of b and r are calculated from equations (27) and (29), respectively.

The results of the numerical solutions for BX–265 and NCFI24–124 are listed in table VII. The BX–265 analysis used the input values for the cell width, aspect ratio, relative density, and stiffness ratio obtained from the LOX block studies, and the NCFI24–124 analysis used the values obtained from the P4 studies. The relative density for each material was obtained from the average densities listed in tables II and III and by assuming a polyurethane solid density ρ_s of 1.2 g/cm^3. The numerical solutions yield the values of the microstructural dimensions r, L, b, and θ.

The value of the predicted cross-section radius from the BX–265 solution is close to the edge cross-section radius measured in the block 2F study, and the value of the predicted NCFI24–124 cross-section radius is close to the edge

NCFI24–124 cross-section radius is close to the edge cross-section radius measured in the P4 study. Note also that the predicted BX–265 edge lengths are close to the edge lengths measured in the block 8E study.

The strength ratio for BX–265 and NCFI24–124 was calculated from equation (19) and the values for the microstructural dimensions r, L, b, and θ, which were obtained from the numerical solution. The predicted strength ratios for both BX–265 and NCFI24–124 compare well with the measured strength ratios.

The values for the Poisson's ratios were calculated from equations (7) and (12). The predicted values for the Poisson's ratio ν_{yx} appear to be significantly lower than the measured value shown in

table IV. Conversely, the predicted values for ν_{yz} and ν_{zy} are significantly higher than the measured values. This is the case for both the BX–265 and NCFI24–124 predictions.

Estimates of the polyurethane modulus E were obtained for BX–265 and NCFI24–124 by comparing the measured rise direction modulus with the predicted rise direction modulus obtained from equation (11) and the solution values for r, L, b, and θ. The same estimate could be obtained by comparing the measured perpendicular-to-rise direction modulus with the predicted modulus obtained from equation (6). The estimated polyurethane moduli for BX–265 and NCFI24–124 are listed in table VII.

TABLE VII.—RESULTS FROM NUMERICAL SOLUTIONS USING ELONGATED KELVIN FOAM MODEL.

		Model results		Measured results	
		BX–265	NCFI24–124	BX–265	NCFI24–124
Input parameters	Cell width, D, μm	136	142		
	Aspect ratio, R	1.42	1.75		
	Relative density, γ	0.031	0.031		
	Stiffness ratio, R_E	1.92	2.94		
Solution results	Cross-section radius, r, μm	22.8	25.2	[a]22.5 [b]18	[c]26
	Edge length, L, μm	61.8	77.2	[b]63	--
	Edge length, b, μm	41.5	35.6	[b]35	--
	Inclination angle, θ, deg	51.33	53.57	--	--
	Strength ratio, R_σ	1.75	2.34	[d]1.82 [e]1.74	[d]2.25 [e]1.99
	Poisson's ratio, ν_{yx}	0.177	0.060	[f]0.355	[f]0.382
	ν_{yz}	.422	.373	[f].273	[f].183 [f].160
	ν_{zy}	.811	1.097	[f].536 [f].675	[f].641
	Solid material Young's modulus, E, GPa	11.0	17.2	--	--
	Vacuum-induced strain,[g] ε_{yy}^*	[h]0.0058	[h]0.0081	[i]0.0067	[i]0.0043
	ε_{zz}^*	[h]–0.0047	[h]–0.0058	[i]–0.0005	[i]–0.0002
	Vacuum-induced change in strength,[g] kPa $\sigma_{yy}^s - \sigma_{yy}^{s,*}$	[h]47.6	[h]60.7	--	49.0[j]
	$\sigma_{zz}^s - \sigma_{zz}^{s,*}$	[h]–69.0	[h]–126.9	--	–25.5[j]

[a]From 2F study.
[b]From 8E study.
[c]From P4 study.
[d]Proportional limit ratio, from table V.
[e]Ultimate strength ratio, from table V.
[f]From table IV.
[g]At less than 3.45 kPa.
[h]Calculated assuming $\sigma_{xx}^* = \sigma_{yy}^* = \sigma_{zz}^* = 1$ atm.
[i]From table VI.
[j]From Morgan (ref. 2).

The strains due to the application of vacuum were calculated using equation (21); the estimated polymer modulus; the solution values for the dimensions L, b, θ, and r; and by assuming that $\sigma_{xx}^* = \sigma_{yy}^* = \sigma_{zz}^* = 1$ atm. The vacuum strain in

the perpendicular-to-rise direction obtained by the BX–265 solution is close to the average measured value of 0.0067. However, the perpendicular-to-rise direction vacuum strain obtained by the NCFI24–124 solution is almost twice the

measured value of 0.0043. Both the BX–265 and NCFI24–124 solutions predicted a negative vacuum strain in the rise direction, a result that is consistent with what was measured in the vacuum strain tests. However, the predicted rise direction strains are considerably higher than the measured values.

The effect of vacuum on the foam tensile strength was calculated using equations (25) and (26) and by assuming $\sigma_{xx}^* = \sigma_{yy}^* = \sigma_{zz}^* = 1$ atm. The predicted results are shown in the last two rows of table VII. The effect of vacuum on the ultimate tensile strength of NCFI24-124 as measured by Morgan (ref. 2) is included for comparison. The predicted effect of vacuum on the perpendicular-to-rise direction strength is close to the measured value. The micromechanics model predicts a strength enhancement in the rise direction, a result that is also consistent with the results obtained by Morgan. However, the magnitude of the predicted strength enhancement is much larger than that which was measured.

It appears that the micromechanics model derived from the open-cell elongated Kelvin model has a tendency to overpredict the rise direction vacuum strain response as well as the effect of vacuum on the rise direction strength. Given that the model also consistently overpredicts the values of the Poisson's ratios ν_{yz} and ν_{zy} and underpredicts the values of ν_{yx}, it is logical to wonder whether the inability of the model to predict the effect of vacuum on the rise direction behavior is somehow related to its inability to predict the Poisson's ratios.

This question can be easily answered by using the measured Poisson's ratios and measured Young's moduli and by applying Hooke's law in the form of equation (20). If it is assumed that $\sigma_{xx}^* = \sigma_{yy}^* = \sigma_{zz}^* = 1$ atm, equation (20) yields values for the vacuum strains for both BX–265 and NCFI24–124, which are quite close to the measured values reported in table VI. We can therefore conclude that if the micromechanics model was capable of predicting the Poisson's ratios, it would also be capable of predicting the vacuum strains.

Finite Element Models of Two BX–265 Elongated Kelvin Unit Cells With and Without Faces

We speculate that the inability of the model to accurately predict the Poisson's ratios stems from our simplifying assumption that the mechanical behavior of the closed-cell space shuttle foams can be simulated using an open-cell model. In reality, the deformation of the cell faces may significantly affect the unit cell displacements in the direction normal to loading. Thus, the presence of the cell faces may have a significant effect on the foam Poisson's ratios.

In order to investigate this possibility, we constructed finite element models of two unit cells: one with cell faces and one without faces. Both finite element models used the BX–265 unit cell dimensions $H = 193$ μm, $D = 136$ μm, $L = 61.8$ μm,

$b = 41.5$ μm, and $\theta = 51.33°$. In the closed-cell model, a uniform thickness of 0.5 μm was assumed for all cell faces.

Finite element analyses were performed using ANSYS (ref. 10). The solid volumes of the cells were modeled using three-dimensional, 10-node tetrahedral (SOLID92) elements. The open-cell model contained 160 000 elements while the closed cell model contained 210 000 elements. Figure 14 shows the open- and closed-cell models.

In both the open- and closed-cell finite element models, the edge cross sections had a three-cusp hypocycloid shape. The edge cross sections were constant along the edge length except at the ends where they were transitioned into the junction points. Unlike the edge cross section illustrated in figure 13, the cusps in the finite element models are not equally spaced by a 120° angle. Instead, the edge cross sections are symmetric about only one axis (see fig. 15), and there are now two cross-section radii, r_α and r_β. A summary of the edge cross-section dimensions for both the open- and closed-cell models is shown in table VIII. Note that the angles between the cusps are not the same for the b-length edges as for the L-length edges. The angles α and β are dictated by the shape of the unit cell. The value of α is larger than the value of β in the b-length edges, whereas $\beta > \alpha$ in the L-length edges. The edge cross-section radii r_α and r_β were selected to ensure that both the open- and closed-cell finite element models had a relative density of 0.031 and to ensure that the L- and b-length edges, in both finite element models, had equal cross-sectional areas. Since the closed-cell model had an additional solid mass contribution from the faces, the edge cross sections in the closed-cell model were smaller than those in the open-cell model.

TABLE VIII.—SUMMARY OF EDGE CROSS-SECTION DIMENSIONS[a] FOR OPEN- AND CLOSED-CELL BX–265 FINITE ELEMENT MODELS.

Model	b-length edges $\alpha = 121°$, $\beta = 119.5°$		L-length edges $\alpha = 104°$, $\beta = 128°$	
	r_α, μm	r_β, μm	r_α, μm	r_β, μm
Open-cell	24.5	23.5	16.1	30
Closed-cell	19.3	18.7	14.0	22.5

[a]See figure 15.

The finite element models were loaded using displacement boundary conditions. Displacement boundary conditions were also applied around the perimeter of the finite element models to maintain the symmetry planes in the deformed state. For example, figure 16(a) shows the loading displacement boundary conditions and the symmetry boundary conditions applied to the open-cell finite element model for loading in the z-direction. In this case, four symmetry planes were established: two that are parallel to the x, z-plane and two that are parallel to the y, z-plane. All nodes that lie within the same symmetry
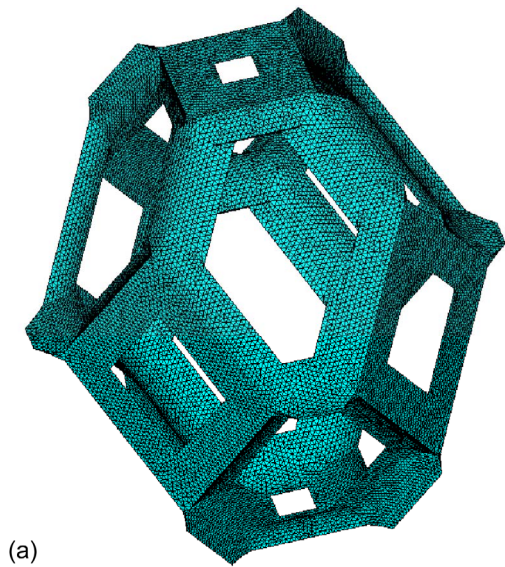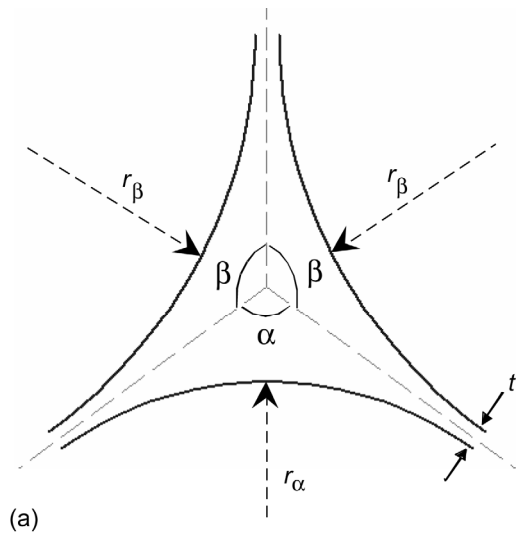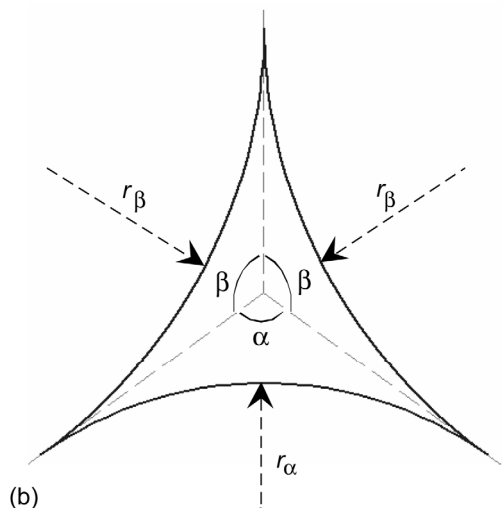
(a)
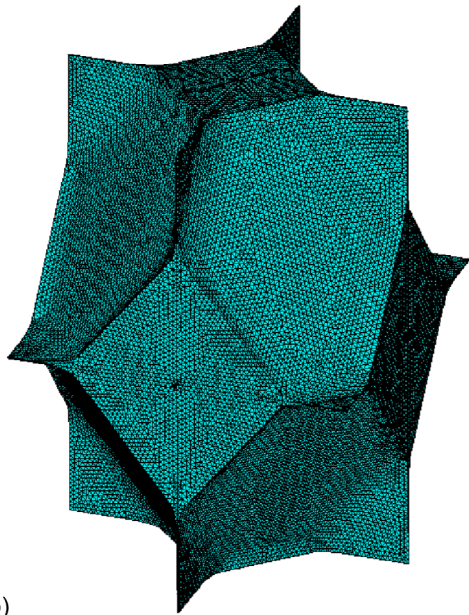
(b)

Figure 14.—Finite element models of elongated
Kelvin unit cell. (a) Open-cell model.
(b) Closed-cell model.

(a)

(b)

Figure 15.—Sketch of three-cusp hypocycloid
edge cross sections for finite element models,
illustrating angles between cusps and two
cross-section radii. (a) Closed-cell edge cross
section. (b) Open-cell edge cross section.

plane were constrained to have the same displacement in the direction normal to the symmetry plane. This was achieved by applying surface contact elements (CONTA174) to all elements falling on a particular symmetry plane. A single target element (TARGE170) was then constructed as a pilot node for the entire plane. The multipoint constraint (MPC) option treats the contact nodes on the contact surface as slave nodes and the pilot node as the master node in the MPC equations. This ensured that the symmetry planes remained planar, that two parallel symmetry planes remained parallel, and that two perpendicular symmetry planes remained perpendicular under the imposed loading. The deformed shape of the open cell finite element model under a z-direction displacement loading Δ_z is illustrated in figure 16(b).
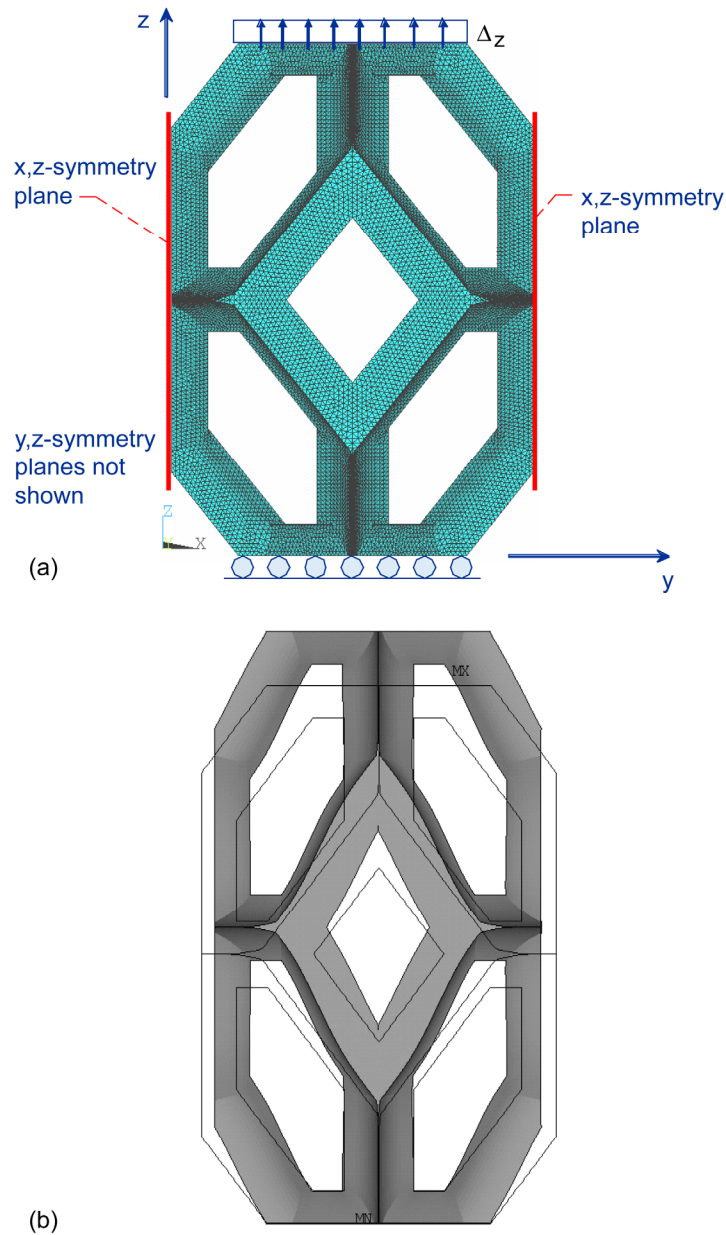
Figure 16.—Displacement load and symmetry boundary conditions
applied to open-cell finite element model for loading in z-direction
and resulting deformed shape. (a) Displacement load and
symmetry boundary conditions. (b) Deformed shape.

The results of the finite element solutions are shown in table IX. The results indicate that including the cell faces has a significant effect on the predicted Poisson's ratios. The effect of including the cell faces is to increase the value of ν_{yx} and to decrease the values of ν_{yz} and ν_{zy}. The Poisson's ratios predicted with the open-cell finite element model compare quite well with the predictions obtained from equations (7) and (12), and the closed-cell finite element model predictions are in close agreement with the measured Poisson's ratios.

Since the presence of the cell faces has a significant influence on the magnitude of the Poisson's ratios, one cannot expect that an open-cell micromechanics model could provide an accurate prediction of the Poisson's ratios for closed-cell foams. Furthermore, it should not be expected to provide an accurate prediction of the magnitudes of the vacuum-induced strains and the magnitudes of the effect of vacuum on the measured strengths. The open-cell model is only capable of predicting the general behavior of closed-cell foams to the effects of vacuum.

TABLE IX.—COMPARISON OF PREDICTED AND MEASURED BX–265 POISSON'S RATIOS.

Poisson's ratio	Predictions using open-cell Kelvin model (closed form solution)[a]	Finite element model predictions		Measured[b]
		Open-cell	Closed-cell	
ν_{yx}	0.177	0.111	0.398	0.355±0.06
ν_{yz}	0.422	0.448	0.236	0.273±0.0007
ν_{zy}	0.811	0.782	0.438	0.536±0.29 0.675±0.17

[a]From table VII.
[b]From table IV.

Conclusion

In this report, we applied the micromechanics model, which was previously developed by the authors for open-cell foams, to model two rigid polyurethane closed-cell foams used on the space shuttle external tank: BX–265 and NCFI24–124. The micromechanics model uses an elongated tetrakaidecahedron as the representative repeating unit cell. The mechanics of deformation of the unit cell led to a set of equations for the modulus, Poisson's ratio, and strength of the foam in the principal material directions. These equations were written in terms of the microstructural dimensions and the strength and stiffness of the solid material.

We have used this same micromechanics model to derive equations that describe the effect of vacuum on the foam mechanical response and strength behavior. Subjecting the closed-cell foams to vacuum results in a differential (internal) pressurization, which induces a tensile stress state in the foam. The micromechanics model leads to equations for the vacuum-induced strains and the effect of vacuum on the tensile strengths in terms of the vacuum-induced stress state σ_{ij}^{*}.

The application of the micromechanics model to BX–265 and NCFI24–124 was encouraging. Using a combination of macroscale measurements (stiffness and relative density) and microstructural measurements (average cell width and average cell aspect ratio) as input, the model and the numerical solution scheme were successful in predicting, to a reasonable level of accuracy, the cell edge lengths and the edge cross-section dimensions. The model also successfully predicted the strength ratios for both foams. The model was not as successful in predicting the Poisson's ratios for either BX–265 or NCFI24–124.

The model predicts the general response of the foams to vacuum exposure, which has been observed in laboratory testing. The model predicts a positive vacuum-induced strain in the perpendicular-to-rise direction and a negative strain in the rise direction. Furthermore, it predicts a reduction in the tensile strength in the perpendicular-to-rise direction and an enhancement in the rise direction strength. Although the model predicted the general response of the foams to the effects of vacuum exposure, it was not able to accurately predict the magnitude of the vacuum effects in the rise direction. This shortcoming is related to the inability of the model to predict the Poisson's ratios. Through the use of finite element analysis, we found that the cell faces had a significant influence on the values of the Poisson's ratios, and thus an open-cell model should not be expected to accurately predict the values of the Poisson's ratios in closed-cell foams.

The aforementioned successes lead us to believe that this micromechanics model can provide a useful tool for understanding the relationship between the foam microstructure and the macroscopic properties. The ability to "jump" between the microscopic and macroscopic scales should prove useful in the structural analysis and structural integrity assessment of foam applications on the External Tank. For example, the model provides us with a tool for predicting foam failure and strength assessment under multiaxial stress states, as it provides us the ability to resolve the combination of stress components into the maximum tensile stress in the most vulnerable edge. Thus, a strength assessment is made by comparing the maximum tensile stress with the tensile strength of the polymer. Future researchers, however, should be cautioned to the inability of the open-cell micromechanics model to predict the Poisson's ratio values for closed-cell foams.

Finally we note that since the relations between the foam microstructure and macroscale properties are in the form of convenient algebraic equations, the stage is set for the development of probabilistic methods to predict the variability in foam material properties in foam applications from a stochastic description of the foam microstructure.

Glenn Research Center
National Aeronautics and Space Administration
Cleveland, Ohio, January 22, 2009

Appendix—Symbols

A	edge cross-sectional area, μm^2
b	cell edge length, μm
C_1	nondimensional constant relating the edge cross-sectional area A to the square of the cross-section radius r
C_2	nondimensional constant relating the edge moment of inertia to $A \cdot r^2$
D	unit cell width, μm
E	solid material Young's modulus, GPa
E_x	foam perpendicular-to-rise direction Young's modulus (along the x-direction), MPa
E_y	foam perpendicular-to-rise direction Young's modulus (along the y-direction), MPa
E_z	foam rise direction Young's modulus (along the z-direction), MPa
H	unit cell height, μm
I	edge moment of inertia, μm^4
I_x^L	moment of inertia of L-length edges about the neutral axis parallel to the unit cell x-axis, μm^4
I_z^b	moment of inertia of b-length edges about the neutral axis parallel to the unit cell z-axis, μm^4
L	cell edge length, μm
M	bending moment
n	number of measurements
R	average cell aspect ratio, H/D
R_E	foam stiffness ratio, $E_z/E_x = E_z/E_y$
R_σ	foam strength ratio, $\sigma_{zz}^s / \sigma_{xx}^s = \sigma_{zz}^s / \sigma_{yy}^s$
r	edge cross-section radius, μm
S	section modulus, μm^3
S_x^L	section modulus of L-length edges about the neutral axis parallel to the unit cell x-axis, μm^3
S_z^b	section modulus of b-length edges about the neutral axis parallel to the unit cell z-axis, μm^3
t	cell face thickness, μm
u	displacement in x-direction

$\overline{u}$	x-direction displacement of unit cell at unit cell boundary (fig. 9).
V	total volume of foam
V_s	volume of foam occupied by solid matter
v	displacement in the y-direction
$\overline{v}$	y-direction displacement of unit cell at unit cell boundary (fig. 9).
w	displacement in the z-direction
$\overline{w}$	z-direction displacement of unit cell at unit cell boundary (fig. 9).
x	Cartesian coordinate perpendicular to the rise direction
y	Cartesian coordinate perpendicular to the rise direction
z	Cartesian coordinate along the rise direction
γ	foam relative density
θ	inclination angle, deg
ε_{xx}^*	strain in perpendicular-to-rise direction (along the x-direction) due to internal pressurization resulting from vacuum
ε_{yy}^*	strain in perpendicular-to-rise direction (along the y-direction) due to internal pressurization resulting from vacuum
ε_{zz}^*	strain in rise direction due to internal pressurization resulting from vacuum
$\nu_{xy} = \nu_{yx}$	foam Poisson's ratios in the plane perpendicular to the rise direction
ν_{zx}	foam Poisson's ratio for strain in the x-direction due to loading in the rise direction
ν_{zy}	foam Poisson's ratio for strain in the y-direction due to loading in the rise direction
ν_{xz}	foam Poisson's ratio for strain in the rise direction due to loading in the x-direction
ν_{yz}	foam Poisson's ratio for strain in the rise direction due to loading in the y-direction
ρ	foam mass density, g/cm^3
ρ_s	mass density of solid material, g/cm^3

σ^s	solid material strength, kPa	σ_{yy}^*	foam tensile stress in the perpendicular-to-rise direction (along y-direction) due to internal pressurization resulting from vacuum exposure, kPa
σ_{yy}	stress in y-direction		
σ_{zz}	stress in rise direction	σ_{zz}^*	foam tensile stress in the rise direction due to internal pressurization resulting from vacuum exposure, kPa
σ_{xx}^s	foam strength in perpendicular-to-rise direction (x-direction), kPa		
σ_{yy}^s	foam strength in perpendicular-to-rise direction (y-direction), kPa	$\sigma_{xx}^{s,*}$	foam perpendicular-to-rise direction strength (along x-direction) in vacuum, kPa
σ_{zz}^s	foam strength in rise direction (z-direction), kPa	$\sigma_{yy}^{s,*}$	foam perpendicular-to-rise direction strength (along y-direction) in vacuum, kPa
σ_{xx}^*	foam tensile stress in the perpendicular-to-rise direction (along x-direction) due to internal pressurization resulting from vacuum exposure, kPa	$\sigma_{zz}^{s,*}$	foam rise direction strength in vacuum, kPa

References

1. Stokes, Eric: Thermal Expansion of Three ET Polyurethane and Polyisocyanurate Foams. SRI–ENG–06–08–11613, 2006.
2. Morgan, K.: Private Communication. NASA Marshall Space Flight Center, May 22, 2006.
3. Sullivan, Roy M.; Ghosn Louis J.; and Lerch Bradley A.: A General Tetrakaidecahedron Model for Open-Celled Foams. Int. J. Solids Struct., vol. 45, 2008, pp. 1754–1765.
4. Zhu, H.X.; Knott, J.F.; and Mills, N.J.: Analysis of the Elastic Properties of Open-Cell Foams With Tetrakaidecahedral Cells. J. Mech. Phys. Solids, vol. 45, no. 3, 1997, pp. 319–343.
5. Wright, Lindsay S.; and Lerch, Bradley A.: Characterization of Space Shuttle Insulative Materials. NASA/TM—2005-213596, 2005.
6. Akabori, Kanji; and Fujimoto, Kazuo: A Method for Measuring Cell Membrane Thickness of Polyurethane Foam. Int. Progress in Urethanes, vol. 2, 1980, pp. 41–60.
7. Schwartz, N.V.; and Bomberg, M.T.: Image Analysis and the Characterization of Cellular Plastics. J. Thermal Insulation, vol. 15, 1991, pp. 153–171.
8. Gibson, Lorna J.; and Ashby, Michael F.: Cellular Solids: Structure & Properties, Pergamon Press, Oxford, England, 1988.
9. Press, William H., et al.: Numerical Recipes in FORTRAN: The Art of Scientific Computing. Second ed., Cambridge University Press, Cambridge, England, 1992.
10. ANSYS 11.0. ANSYS, Inc., Canonsburg, PA, 2007.

REPORT DOCUMENTATION PAGE					Form Approved OMB No. 0704-0188

The public reporting burden for this collection of information is estimated to average 1 hour per response, including the time for reviewing instructions, searching existing data sources, gathering and maintaining the data needed, and completing and reviewing the collection of information. Send comments regarding this burden estimate or any other aspect of this collection of information, including suggestions for reducing this burden, to Department of Defense, Washington Headquarters Services, Directorate for Information Operations and Reports (0704-0188), 1215 Jefferson Davis Highway, Suite 1204, Arlington, VA 22202-4302. Respondents should be aware that notwithstanding any other provision of law, no person shall be subject to any penalty for failing to comply with a collection of information if it does not display a currently valid OMB control number.
PLEASE DO NOT RETURN YOUR FORM TO THE ABOVE ADDRESS.

1. REPORT DATE (DD-MM-YYYY) 01-01-2009	2. REPORT TYPE Technical Paper	3. DATES COVERED (From - To)

4. TITLE AND SUBTITLE Elongated Tetrakaidecahedron Micromechanics Model for Space Shuttle External Tank Foams	5a. CONTRACT NUMBER
	5b. GRANT NUMBER
	5c. PROGRAM ELEMENT NUMBER
6. AUTHOR(S) Sullivan, Roy, M.; Ghosn, Louis, J.; Lerch, Bradley, A.; Baker, Eric, H.	5d. PROJECT NUMBER
	5e. TASK NUMBER
	5f. WORK UNIT NUMBER WBS 524238.08.02.03.04

7. PERFORMING ORGANIZATION NAME(S) AND ADDRESS(ES) National Aeronautics and Space Administration John H. Glenn Research Center at Lewis Field Cleveland, Ohio 44135-3191	8. PERFORMING ORGANIZATION REPORT NUMBER E-16293

9. SPONSORING/MONITORING AGENCY NAME(S) AND ADDRESS(ES) National Aeronautics and Space Administration Washington, DC 20546-0001	10. SPONSORING/MONITORS ACRONYM(S) NASA
	11. SPONSORING/MONITORING REPORT NUMBER NASA/TP-2009-215137

12. DISTRIBUTION/AVAILABILITY STATEMENT
Unclassified-Unlimited
Subject Categories: 27, 39, 18, and 64
Available electronically at http://gltrs.grc.nasa.gov
This publication is available from the NASA Center for AeroSpace Information, 301-621-0390

13. SUPPLEMENTARY NOTES

14. ABSTRACT
The results of microstructural characterization studies and physical and mechanical testing of BX-265 and NCFI24-124 foams are reported. A micromechanics model developed previously by the authors is reviewed, and the resulting equations for the elastic constants, the relative density, and the strength of the foam in the principal material directions are presented. The micromechanics model is also used to derive equations to predict the effect of vacuum on the tensile strength and the strains induced by exposure to vacuum. Using a combination of microstructural dimensions and physical and mechanical measurements as input, the equations for the elastic constants and the relative density are applied and the remaining microstructural dimensions are predicted. The predicted microstructural dimensions are in close agreement with the average measured values for both BX-265 and NCFI24-124. With the microstructural dimensions, the model predicts the ratio of the strengths in the principal material directions for both foams. The model is also used to predict the Poisson's ratios, the vacuum-induced strains, and the effect of vacuum on the tensile strengths. However, the comparison of these predicted values with the measured values is not as favorable.

15. SUBJECT TERMS
Polymeric foam; Non-isotropic; Elongated tetrakaidecahedron (Kelvin) model; Foam material; Elastic material; Energy methods; Microstructural characterization; Mechanical testing

16. SECURITY CLASSIFICATION OF:			17. LIMITATION OF ABSTRACT	18. NUMBER OF PAGES	19a. NAME OF RESPONSIBLE PERSON STI Help Desk (email:help@sti.nasa.gov)
a. REPORT U	b. ABSTRACT U	c. THIS PAGE U	UU	29	19b. TELEPHONE NUMBER (include area code) 301-621-0390

Standard Form 298 (Rev. 8-98)
Prescribed by ANSI Std. Z39-18